ACES Asian Chemical Editorial Society

DOI: 10.1002/cnma.201900404

CHEMNANOMAT
Full Paper

# Enhanced Photo-Response of $Mos_2$ Photodetectors by a Laterally Aligned $SiO_2$ Nanoribbon Array Substrate

Namsoo Lim[+],[a] Yusin Pak[+],[a] Jae-Keun Kim,[b] Tae Jin Yoo,[a] Hyeonghun Kim,[a] Yogeenth Kumaresan,[a] Woochul Kim,[a] Seongjun Cho,[a] Sooncheol Kwon,[c] Byoung Hun Lee,[a] Takhee Lee,*[b] and Gun-Young Jung*[a]

**Abstract:** Achieving both high photocurrent and small dark current is required for the enhanced performance of molybdenum disulfide ($MoS_2$) photodetector (PD). In the two-dimensional transition metal dichalcogenide PD, inevitable recombinations occur highly at intrinsic defects of $MoS_2$ and impede photo-generated carrier releasement into electrodes, resulting in a poor PD performance. To address this issue without introducing a superiorly high-crystalline $MoS_2$ monolayer and/or complex PD architecture, we for the first time report a facile method of simply transferring the $MoS_2$ onto a periodically aligned silicon dioxide nanoribbons (SNR) array substrate fabricated by 325 nm laser interference lithography. Interestingly, two different *n*-doping states are arranged alternately on the $MoS_2$ layer, depending on the underlying region of contact substrate (pristine $SiO_2$ and SNR). The different *n*-doping levels induce internal electric fields by which photo-generated carriers are separated, reducing the recombination chance. The $MoS_2$ PD on the SNR array substrate shows an improved photocurrent to dark current ratio of ~360 (~7 times larger than that of the reference PD on the pristine $SiO_2$ substrate), while producing a small dark current of $\sim 10^{-12}$ A at $V_G = 0$ V. Our method paves the way for enhancing the performance of other 2D materials-based optoelectronic devices.

## 1. Introduction

As the first demonstrated two-dimensional (2D) material,[1] graphene attracted tremendous attentions in many fields. Superb electronic, thermal, mechanical, optical properties of the graphene (*e.g.*, a mobility of 200,000 $cm^2/V\,s$,[2] a thermal conductivity of 5,000 W/mK,[3] and an excellent strength of 42 N/m,[4] etc.) had been demonstrated in a relatively short time, inducing many follow-up application studies.[5] However, as the graphene has zero bandgap[1] and a low light absorption coefficient,[6] it is difficult to be used as a semiconductor in the field of optoelectronics. Therefore, 2D transition metal dichalcogenides (TMDs) with tunable bandgaps[7] were emerged as a notable material to overcome the disadvantages of the graphene.[8]

2D-molybdenum disulfide (hereafter $MoS_2$) is one of the most widely investigated TMDs. It is an atomically-thin membrane (0.65 nm-thick) consisting of a layer of molybdenum (Mo) atoms sandwiched by sulfur (S) atoms. The strong covalent bond[9] emerging from the sandwiched structure is the source of superior mechanical flexibility, strong hardness (30 times stronger than steel), and high thermal stability (up to ~1100 °C under inert atmosphere).[10] Above all, it possesses an energy bandgap which is tunable from 1.2 (bulk) to 1.8 eV (monolayer) depending on the number of layers.[11] Besides, its high absorption coefficient makes it very promising for optoelectronic devices,[12,13,14] such as photodetectors (PDs),[15,16,17] light emitters,[18] photovoltaic cells,[19,20] etc.

In the early stage of research, excellent performances of $MoS_2$ PDs (*e.g.*, a high photo-responsivity of 880 A/W[16]) were demonstrated with complicated device architectures. However, there are several issues still remained; (*i*) high dark-current,[12,16,21] (*ii*) large recombination,[22] etc. To resolve these issues, split-gate electrodes were used in TMDs PDs.[12,21,23,24] Applying one gate (located underneath a TMD/dielectric layer) with a negative voltage and the other with a positive voltage effectively induced holes and electrons within the TMD channel around anode and cathode, respectively. Therefore, the built *p-n* junction enabled a small dark current at a strong reverse bias. Unfortunately, however, this method is not suitable for $MoS_2$ devices because the intrinsically strong *n*-type nature of pristine $MoS_2$ rendered it difficult in obtaining an appropriate *p*-doped state by the electrostatic doping.[16] Moreover, complex fabrication and relatively large power consumption were critical problems to be urgently solved for practical optoelectronic applications.[21,23,24]

[a] *Dr. N. Lim,[+] Dr. Y. Pak,[+] T. J. Yoo, H. Kim, Dr. Y. Kumaresan, W. Kim, S. Cho, Prof. B. Hun Lee, Prof. G.-Y. Jung*
*School of Materials Science and Engineering*
*Gwangju Institute of Science and Technology (GIST)*
*Gwangju 61005 (Republic of Korea)*
*E-mail: gyjung@gist.ac.kr*

[b] *J.-K. Kim, Prof. T. Lee*
*Department of Physics and Astronomy*
*Institute of Applied Physics*
*Seoul National University*
*Seoul 08826 (Republic of Korea)*
*E-mail: tlee@snu.ac.kr*

[c] *Dr. S. Kwon*
*Research Institute for Solar and Sustainable Energies*
*Gwangju Institute of Science and Technology (GIST)*
*Gwangju 61005 (Republic of Korea)*

[+] *These authors equally contributed.*

Supporting information for this article is available on the WWW under https://doi.org/10.1002/cnma.201900404

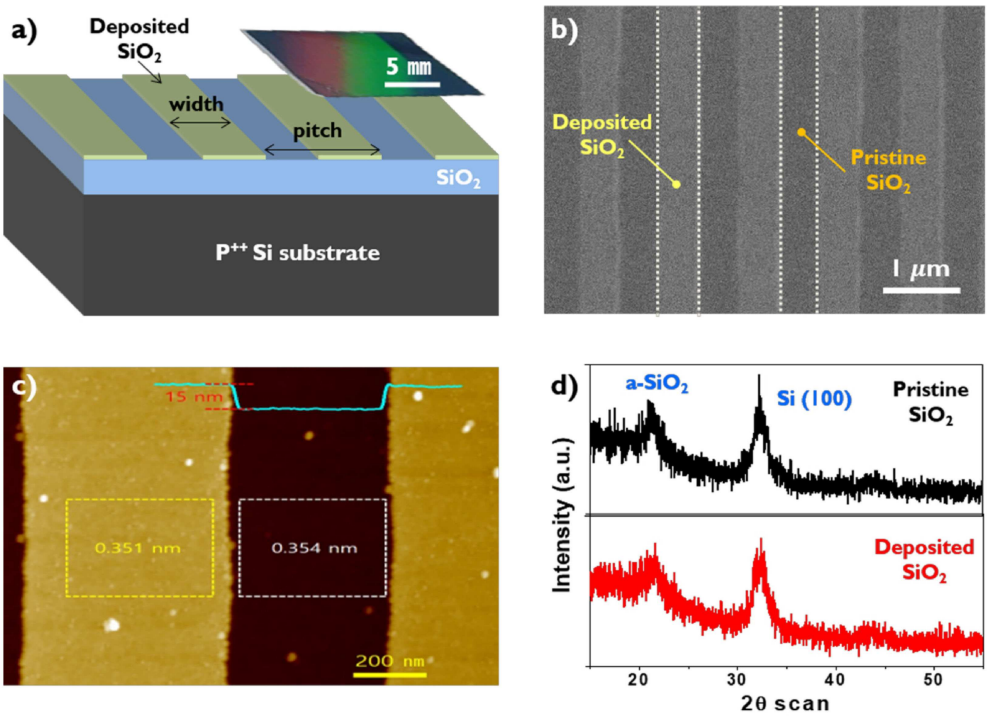


**Figure 1.** Characterizations of the SNRs substrate. (a) The schematic image of the SNRs substrate (inset; an actual photo of the SNRs substrate at an area of 2.25 $cm^2$). (b) The SEM and (c) AFM images of the fabricated SNRs substrate (at 1 μm pitch). (d) Comparison of X-ray diffraction (XRD) spectra of the pristine $SiO_2$ and e-beam deposited $SiO_2$.

Achieving a high photocurrent is another prerequisite for enhanced performance of $MoS_2$ PD. In this regard, photo-generated electron-hole pairs' recombination[22] that gives bad influence to photocurrent, needs to be importantly considered. The inevitable recombinations occur highly at intrinsic defects of $MoS_2$ such as grain boundaries, interstitials, dislocations, etc., and impede the releasement of photo-generated electron-hole pairs (hereafter photo-generated carriers) into electrodes, resulting in a poor photocurrent. Therefore, to simultaneously achieve both goals (high photocurrent and small dark current) without introducing a superiorly high-crystalline $MoS_2$ mono-layer and/or complex PD architecture, it is necessary to develop a breakthrough PD architecture for efficient separation and releasement of photo-generated carriers.

In this work, we demonstrate that a doping state of $MoS_2$ can be modulated by the material in contact with it[25,26] and the substrate morphology fabricated by 325 nm laser interference lithography (LIL) process.[27] We show a facile method to efficiently separate photo-generated carriers, simply by transferring a $MoS_2$ onto a periodically aligned silicon dioxide nanoribbon (SNR) array substrate. Interestingly, two different surface potentials (~$\Delta$20 mV) are formed on the transferred $MoS_2$ layer, indicating that the *n*-doping level is locally different depending on underlying substrate region (in contact with pristine $SiO_2$ or SNR). The different *n*-doping levels of two neighboring $MoS_2$ regions can induce an internal electric field. Thus, photo-generated carriers are effectively separated and swept farther from each other, reducing the recombination chance. To see the effect of SNR array direction on the efficiency of photo-generated carriers, two substrates with SNRs residing laterally and vertically to current flow direction are prepared. Photo-responses of these two PDs (on lateral and vertical SNRs substrates) are compared with the reference PD fabricated on the pristine $SiO_2$ substrate.

## 2. Results and Discussion

Figure 1a shows a schematic of the SNRs substrate fabricated by the LIL process and subsequent $SiO_2$ deposition technique. The LIL process is very useful for fabricating periodically aligned nano-patterns (*e.g.*, line-, dot-, and hole array) in a relatively large area (Supporting Information, Figure S1). The inset figure (in Figure 1a) is an actual photo image of the SNRs substrate with an area of 2.25 $cm^2$, exhibiting iridescent colors owing to the periodicity of pattern. Figure 1b shows a top-view image of the superiorly aligned SNRs with a width of 540 nm at 1 μm pitch, measured by a scanning electron microscope (SEM).

Two regions (bright and dark) of Figure 1b correspond to e-beam deposited SNR and pristine $SiO_2$ which are alternately arranged over the whole substrate. The surface morphology and roughness of the SNRs substrate were characterized using an atomic force microscope (AFM). The thickness of the SNR was measured to be 15 nm (Figure 1c). The root-mean-square (RMS) roughness values were 0.354 nm and 0.351 nm, respectively for the SNR and pristine $SiO_2$ surfaces, indicating that the morphology and/or roughness effect on the contact *n*-doping can be almost excluded. To confirm the composition and

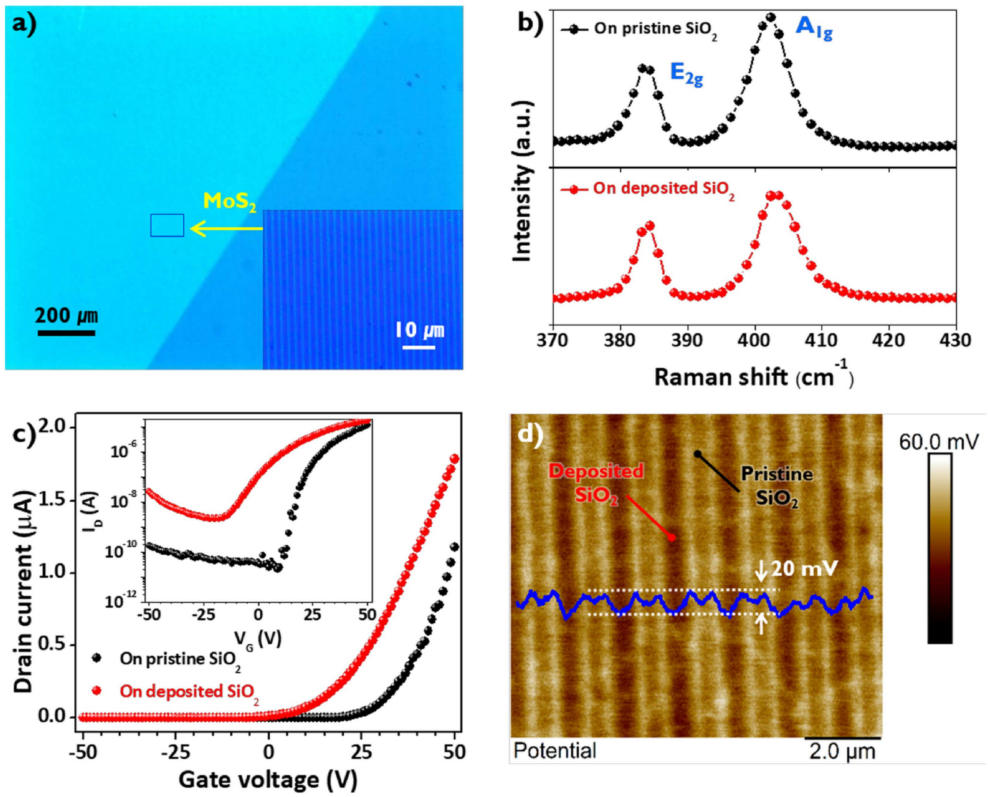


**Figure 2.** The SNRs substrate-induced contact *n*-doping into the superjacent $MoS_2$ monolayer. (**a**) Optical microscope (OM) image of the $MoS_2$ monolayer transferred onto the SNRs substrate (inset; OM image at a high magnification, showing the underlying periodically aligned SNRs). (**b**) Raman spectra of the $MoS_2$ monolayers transferred onto the pristine $SiO_2$ and e-beam deposited-$SiO_2$ substrates. (**c**) Transfer characteristics ($I_D$-$V_G$ curves) of the $MoS_2$ FETs fabricated on the pristine $SiO_2$ and e-beam deposited-$SiO_2$ substrates. (**d**) Surface potential mapping of the transferred $MoS_2$ monolayer on the SNRs substrate.

crystallinity of the SNRs, X-ray diffraction (XRD) measurement was performed. Both SNR and pristine $SiO_2$ possess characteristic XRD peaks of amorphous $SiO_2$ and crystalline Si (100), as plotted in Figure 1d. Any significant change in peak position, intensity, and background noise was not found.

A chemical vapor deposition (CVD)-grown $MoS_2$ monolayer was transferred onto the SNRs substrate *via* wet-transfer method.[28] The transferred $MoS_2$ monolayer as shown in Figure 2a has an area of ~0.6 $mm^2$ without any noticeable wrinkle, rupture, and contamination, observed by an optical microscope (OM). The inset image (in Figure 2a) obviously shows the aligned SNRs beneath the transferred $MoS_2$ monolayer. To find changes in molecular bonds and electronic states of the $MoS_2$ monolayer (after transferring onto the SNRs and pristine $SiO_2$ substrates, respectively), Raman spectroscopy using an excitation wavelength of 514 nm was conducted. Both SNRs and pristine $SiO_2$ substrates presented the inherent peaks of $MoS_2$ at around 383 $cm^{-1}$ and 407 $cm^{-1}$, corresponding to in-plane ($E_{2g}$) and out-of-plane ($A_{1g}$) mode vibrations, respectively, as shown in Figure 2b. The peak distance between $E_{2g}$ and $A_{1g}$ was approximately 19.2 $cm^{-1}$, which can be a shred of definite evidence for the $MoS_2$ monolayer.[29] Except for a tiny shift of peak, any significant change was not found in the Raman spectra.

Bottom-gated $MoS_2$ field effect transistors (FETs) were fabricated to demonstrate the contact *n*-doping effect from a dielectric layer (either pristine $SiO_2$ or e-beam deposited $SiO_2$) to the transferred $MoS_2$. Figure 2c shows the *n*-type transfer curves of $MoS_2$ FETs fabricated on the pristine $SiO_2$ and e-beam deposited $SiO_2$ dielectrics. The threshold voltage ($V_{th}$) was fairly shifted from 30 V (pristine $SiO_2$) to 15 V (e-beam deposited $SiO_2$). The drain current ($I_D$) of the e-beam deposited $SiO_2$ device was elevated in the entire gate voltage ($V_G$) range (inset: on a logarithmic scale). These $I_D$-$V_G$ characteristics indicate that the contact *n*-doping can be very effective and useful to increase electron density in the $MoS_2$ channel.[30] It was previously reported that such e-beam deposited $SiO_2$ is prone to be stoichiometrically oxygen ($O_2$) deficient, thus generating more free electrons which can contribute to the efficient contact *n*-doping.[31] The bright surface color of the e-beam deposited $SiO_2$ region (as shown in Figure 1b) is an indirect evidence for the increased electron density.

To find a direct clue for the contact *n*-doping to the $MoS_2$, Kelvin probe force microscopy (KPFM) was performed. Figure 2d exhibits a 2D colored map of surface potentials distributing on the $MoS_2$ monolayer placed on the SNRs substrate. In general, a contact potential difference (CPD) is obtained by measuring a voltage that nullifies an oscillating electrostatic force between a probe tip and sample surface. On average, the surface potential

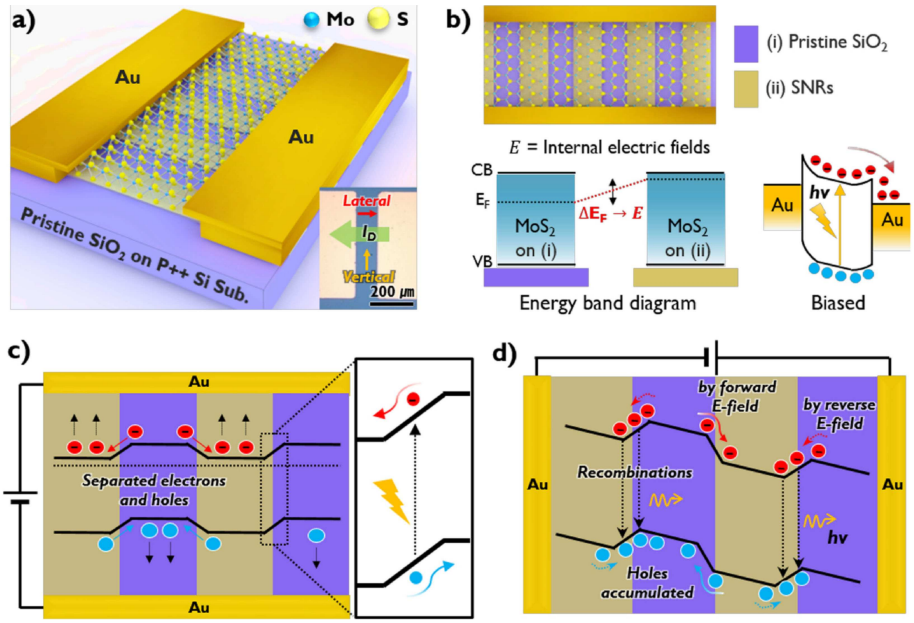


**Figure 3. (a)** Schematic image of the FET-type $MoS_2$ PD fabricated on the SNRs substrate, and the OM image of the actual PD channel (inset). 'Lateral' and 'Vertical' indicate the alignment direction of the SNRs which is labeled based on the $I_D$ flow direction. (**b**) Tow-view schematic image of the lateral SNRs PD and the corresponding energy band diagram of each region having a different surface potential. The difference in the contact n-doping level is the source of the E-field. Under illumination, photo-generated carriers can be easily released into electrodes. (**c**) Efficient and prompt separation of photo-generated carriers by the E-fields in the case of lateral SNRs PD. (**d**) In the case of vertical SNRs PD, electrons and holes flow in two directions: forward or reverse to the external $V_{DS}$.

of the $MoS_2$ on the SNRs region (bright) is higher than that on the pristine $SiO_2$ region (dark), indicating more free electrons in the bright region (on the SNRs) owing to a high contact *n*-doping. The potential difference between the dark region and the bright region was ~20 mV (along the line profile) which is considered enough for efficient separation of electron-hole pairs.[32] For comparison, the CPD on the SNRs substrate (without the $MoS_2$) was not measured due to the insulating property of $SiO_2$ (Supporting Information, Figure S2).

Figure 3a presents a schematic of FET-type $MoS_2$ PD with a channel length of 100 $\mu$m (inset figure). We hypothesized that the separation of photo-generated carriers can be markedly enhanced when the alignment direction of SNRs is the same with the $I_D$ flow direction of the FET-type $MoS_2$ PD (hereafter we call this device 'lateral PD'). If the SNRs reside vertically to the $I_D$ flow direction, it is called 'vertical PD'. Figure 3b shows the schematic image, band structure, and band diagram of the lateral PD. In the lateral PD, two neighboring $MoS_2$ regions with different contact *n*-doping states reside alternately on the underlying (*i*) pristine $SiO_2$ and (*ii*) SNRs, as shown in the top-view schematic of the PD channel (Figure 3b). As demonstrated by the KPFM result (Figure 2d), the $MoS_2$ region on the SNR is locally more *n*-doped than that on the pristine $SiO_2$, as depicted in the energy band diagram of Figure 3b. Therefore, the difference in their Fermi energies can promote spontaneous charge transfer,[33–36] generating an internal electric fields (E-fields) at every boundary of two neighboring $MoS_2$ regions. Upon illumination, photo-generated carriers are separated by the E-fields, and thus they are easily released into electrodes under an external $V_{DS}$ (when biased in Figure 3b). Figure 3c is a schematic of the E-fields continuously distributing up-and-down at the vicinity of SNRs within the lateral PD channel. If the lateral PD is illuminated, photo-generated electrons and holes at the boundaries are efficiently driven by the E-fields. In principle, keeping electrons and holes farther apart from each other until they reach their corresponding electrodes, is very beneficial for decreasing recombination chance, which can notably contribute to the increase in a total photocurrent ($I_{ph}$). For comparison, we also prepared the vertical PD where the SNRs are aligned vertically to the $I_D$ flow direction (Figure 3d). Under the illumination, the photo-generated carriers are separated and driven by the E-field in two directions; forward or reverse to the external $V_{DS}$. The forward E-field shoves electrons to the edge of reverse E-field and the electrons are likely to recombine with the accumulated holes there. The reverse E-field offsets the overall current. Thus, the $I_{ph}$ would be fairly reduced and unstable.

To verify the efficient separation of photo-generated carriers by the E-fields, we prepared four $MoS_2$ PDs on various substrates; (*i*) pristine $SiO_2$, (*ii*) e-beam deposited $SiO_2$, (*iii*) lateral SNRs, and (*iv*) vertical SNRs. Figure 4 shows the transfer curves of the four PDs measured at $V_D = 8$ V before and after illumination. In the case of pristine $SiO_2$ PD (Figure 4a), typical *n*-type $I_D$-$V_G$ characteristics with the $V_{th}$ of ~8 V was confirmed. Under a power density ($P_d$) of ~75 mW/cm$^2$, $I_D$ increased in the whole $V_G$ range, exhibiting $I_{ph}$ of $1.19\times10^{-10}$ A, dark current ($I_{dark}$) of $2.2\times10^{-12}$ A, and thus the ratio of $I_{ph}$ to $I_{dark}$ of ~54 at $V_G = 0$ V. In the case of e-beam deposited $SiO_2$ PD (Figure 4b),

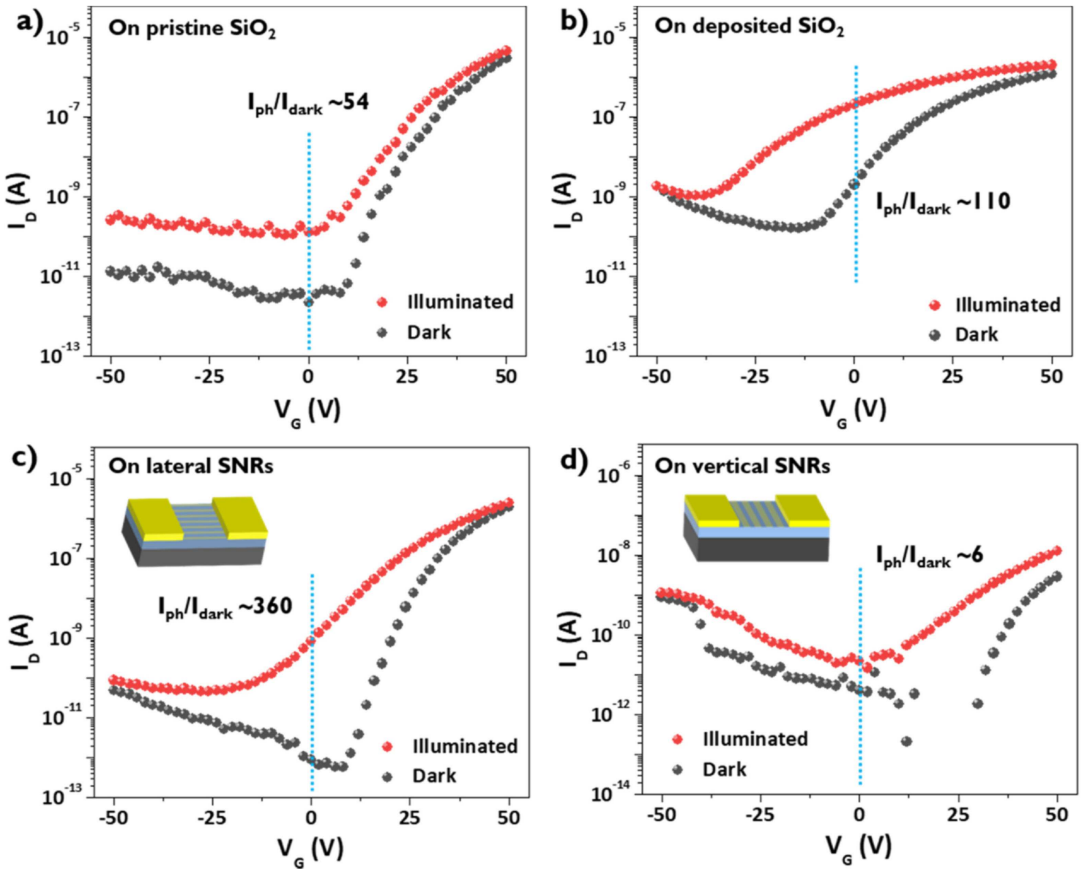


**Figure 4.** Transfer characteristics of the FET-type $MoS_2$ PDs fabricated on the (**a**) pristine $SiO_2$, (**b**) e-beam deposited $SiO_2$, (**c**) lateral SNRs, and (**d**) vertical SNRs substrates. The PD performance of each device was measured at $V_D = 8$ V under a $P_d$ of 75 mW/cm$^2$. Inset images in Figure 4c and d depict the $MoS_2$ PDs fabricated on the lateral SNRs and vertical SNRs substrates, respectively.

the $V_{th}$ was negatively shifted. Both $I_{ph}$ and $I_{dark}$ values (*e.g.*, $I_{dark}$ of $1.99\times10^{-9}$ A and $I_{ph}$ of $2.19\times10^{-7}$ A, at $V_G = 0$ V) were increased in the whole $V_G$ range compared to those of the pristine $SiO_2$ PD. Although the $I_{ph}/I_{dark}$ was increased up to ~110, the increased $I_{dark}$ owing to the high contact *n*-doping can cause a shot noise and background signal fluctuation.[12,16,21] In the case of lateral SNRs PD (as illustrated in Figure 4c inset), the $I_{dark}$ (*e.g.*, $\sim8.81\times10^{-13}$ A at $V_G = 0$ V) was slightly smaller than that of the pristine $SiO_2$ PD. This lower $I_{dark}$ level would probably be associated with the contact resistance of 2D-TMD on the patterned morphology of the SNRs substrate. Furthermore, the $I_{ph}/I_{dark}$ was ~360 at $V_G = 0$ V, which is approximately 7 times larger than that of the pristine $SiO_2$ PD. This large enhancement is due to the efficient separation of photo-generated electron-hole pairs by the E-fields. In contrast, the vertical SNRs PD exhibited unstable $I_{dark}$ and small $I_{ph}$ values, yielding the $I_{ph}/I_{dark}$ of ~6, as shown in Figure 4d. The poor photo-response characteristics of the vertical SNRs PD is because the flow of photo-generated carriers is hindered by the reverse E-fields while crossing the boundaries. The combined effect of separated electrons' perturbation and more recombination chance is the main reason for the bad and unstable PD performance. The characteristics of these four $MoS_2$ PDs well support our hypothesis.

To compare photo-response efficiencies of three PDs (fabricated on the pristine $SiO_2$, the lateral SNRs, and the vertical SNRs substrates, respectively), photo-responsivity ($R_{ph}$) was calculated by extracting necessary parameters from the transfer curves of Figure 4. The $R_{ph}$ was defined by the following formula:

$$R_{ph} = I_{ph}/P_d \cdot A \quad (1)$$

where $P_d$ is the power density, and A is the illuminated active area within the PD channel. Figure 5a shows a plot of $R_{ph}$ as the function of $V_G$ from −20 V to 20 V in 5 V interval under the $P_d$ of 75 mW/cm$^2$. Overall, the $R_{ph}$ values of three PDs increased linearly with the $V_G$ (> 0 V). This linearity is generally hindered by defect sites, as they can severely disturb the drift of electrons and holes at low voltages.[38–40] At $V_G = 0$ V, the $R_{ph}$ values were 3.1, 21, and 0.46 $\mu$A/W for the pristine $SiO_2$ PD (Figure 4a), lateral SNRs PD (Figure 4c), vertical SNRs PDs (Figure 4d), respectively. In the lateral SNRs PD, the enhancement in $I_{ph}$ was remarkable with a $V_G$ increment. At $V_G = 20$ V, the $R_{ph}$ values were 315, 1630, and 5.22 $\mu$A/W for the pristine $SiO_2$, the lateral SNRs PD and the vertical SNRs PD, respectively. These values are acceptable considering the long channel length of 100 $\mu$m, where a significant loss of photo-generated carriers is expected

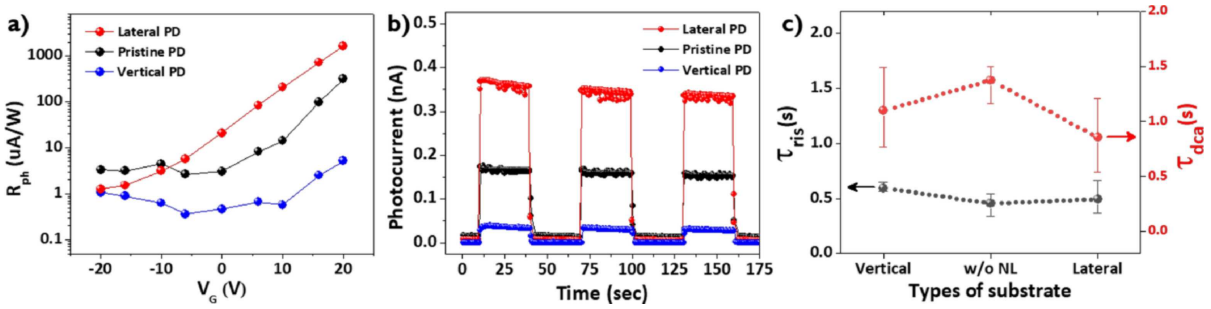


**Figure 5. (a)** Photo-responsivity of each MoS2 PD (on lateral SNRs, vertical SNRs, and pristine SiO2 substrates) as a function of VG. **(b)** Transient photo-responses of the aforementioned three PDs as a function of time, showing square rise and decay behaviors. **(c)** Comparison of τ_ris andτ_dca values of the three PDs.

**Table 1.** $\tau_{ris}$ and $\tau_{dca}$ values of other PDs reported in the pertinent literature.

| Device | Fabrication | Channel length [um] | $V_D$ [V] | $V_G$ [V] | Wavelength [nm] | Intensity [mW/cm$^2$] | $\tau_{ris}$ [ms] | $\tau_{dca}$ [ms] |
|---|---|---|---|---|---|---|---|---|
| [16]1 L $MoS_2$ | Mechanical exfoliation | ~5 | 8 | −70 | 561 | 0.024 | $4\times10^3$ | $9\times10^3$ |
| [15]1 L $MoS_2$ | Mechanical exfoliation | 2.1 | 1 | 50 | 670 | 0.08 | 50 | 50 |
| [42]1 L $MoSe_2$ | CVD | ~15 | 5 | *nr* | 532 | 50 | 60 | 60 |
| [43]1 L $MoS_2$ | CVD | ~10 | 1 | ~41 | 532 | 1.08 | $5\times10^5$ | 3000 |
| [44]Multi layered $MoS_2$ | Chemical exfoliation | ~4 | 8 | 0 | 532 | *nr* | 500 | 700 |
| [40]Multi layered $MoS_2$ | Mechanical exfoliation | 3 | 1 | 0 | 280~750 | 100 | $5\times10^3$ | $6.5\times10^4$ |
| 1 L $MoS_2$ (This work) | CVD | 100 | 8 | 0 | 400~800 | 75 | 620 | $\sim1\times10^3$ |

*nr* = not reported, ~ = approximately

due to the higher recombination chance while moving along the long channel.

Figure 5b represents cyclic photo-responses of three PDs (on the pristine $SiO_2$, the lateral SNRs, and the vertical SNRs substrates). In each measurement, three cycles (30 sec for ON and 30 sec for OFF) were given at $V_D = 8$ V and $V_G = 0$ V. All three PDs exhibited reliable photo-responses with complete on-off cycles. Overall, the similar photo-response tendency to the results of the transfer characteristics discussed in figure 4 was observed. The lateral SNRs PD demonstrated the superiorly enhanced $I_{ph}$ values compared to the reference PDs. In addition, the cyclic photo-response of the e-beam deposited $SiO_2$ PD was measured. In this case, the $I_{ph}$ was not saturated properly in a given time due to a slow increment of $I_{ph}$ and the photo-response signal was severely noisy (Supporting Information, Figure S3). Rise ($\tau_{ris}$) and decay ($\tau_{dca}$) times are one of the major figures of merit for developing a high speed PD. To precisely extract the time components, a single exponential function with the following formula ($y = y_0 + A_1 e^{-(x-x_0)/t_1}$) was used (Supporting Information, Figure S4). The extracted $\tau_{ris}$ and $\tau_{dca}$ of the lateral SNRs PD (Figure 5c) are 620 ms and 1030 ms, respectively. The same extraction method was used to achieve the $\tau_{ris}$ and $\tau_{dca}$ values of the pristine $SiO_2$ PD and the vertical SNRs PD. Their $\tau_{ris}$ and $\tau_{dca}$ values were not much different among those. For comparative analysis, the $\tau_{ris}$ and $\tau_{dca}$ values of PDs in the pertinent literature were surveyed. Considering larger dimensions of our PDs and dial-operating lamp used for the illumination, which could negatively affect the $\tau_{ris}$ and $\tau_{dca}$, we believe that the $\tau_{ris}$ and $\tau_{dca}$ values of our PDs are within the reasonable range of performance (Table 1).

## 3. Conclusion

We, for the first time, reported the enhanced PD performance based on the different contact *n*-doping states formed on the $MoS_2$ monolayer, simply by using the SNRs substrate fabricated by the LIL process. Different surface potentials (~Δ20 mV) were made on the same transferred $MoS_2$ monolayer depending on the underlying region of contact substrate; the pristine $SiO_2$ and the SNR. The difference of *n*-doping levels between the two neighboring regions of $MoS_2$ induced the E-fields, which efficiently separated the photo-generated carriers farther from each other and thus reduced recombination chance. Therefore, upon illumination, the lateral SNRs PD exhibited the remarkable improvement in the $I_{ph}/I_{dark}$ value (~360) which is approximately 7 times larger than that of the pristine $SiO_2$ PD along with the low $I_{dark}$ (*e.g.*, $\sim10^{-12}$ A at $V_G = 0$ V). Our practical and facile *n*-doping method could greatly contribute to developing high-performance 2D-TMDs PDs that can be equipped or embedded into next-generation optoelectronic devices.

## Experimental Section

*Fabrication of the SNRs substrates*: A pitch-tunable SNR substrate was fabricated via 325 nm He–Cd laser interference lithography (LIL) process (See the SI Figure S5). A 300 nm-thick $SiO_2$/Si wafer ($p^{++}$-doped Si, QL Electronics Co., China) was cleaned sequentially in acetone, isopropyl alcohol, and deionized water in ultrasonic bath for 10 min each. A bottom antireflection coating layer (100 nm thick, AZ BARLi-II 90, MicroChemicals GmbH, Germany) and a negative-tone photoresist (350 nm thick, AZ nLOF 2020, Micro-

Chemicals) were spin-coated in sequence at 4000 rpm for 40 sec each, followed by 1 min soft-baking at 110 °C. The sample was exposed to the interference light of 325 nm laser, and developed in a developing solution (AZ 300 MIF, MicroChemicals) to produce photoresist line patterns. The exposed parts of the BARC layer were etched away by $O_2$ plasma process. Then, 15 nm-thick $SiO_2$ was deposited by e-beam evaporation, and the photoresist/BARC layers were eliminated by immersing in a lift-off solution (EKC 830, DuPont, USA), leaving the SNRs on the substrate. The sample underwent a high temperature annealing (at 900 °C for 3 hrs) not only to relieve stresses which might emerge during the deposition, but also to eliminate organic impurities.

*Fabrication of the FET-type $MoS_2$ PDs*: A piece of CVD-grown $MoS_2$ monolayer was transferred onto the prepared SNRs substrate by a wet-transfer method.[41] Prior to the transfer, the substrate surface was rendered hydrophilic by a short time $O_2$ plasma treatment, which was beneficial for good adhesion, because the $MoS_2$ transfer is performed in water. To enhance the adhesion between the $MoS_2$ and $SiO_2$ substrate, the sample underwent vacuum annealing at 300 °C for 1 hr. Then, 80 nm-thick Au was deposited via e-beam evaporation using a shadow mask to construct source-drain electrodes on the transferred $MoS_2$ monolayer.

*Photo-response characterization of the $MoS_2$ PDs*: Transfer curves and transient photo-responses were measured by a probe-station (MST 5500B, MS TECH, South Korea) equipped with a Keithley 4200 system for I–V analysis. A back-gate contact to $p^{++}$-doped silicon exposed by scratching the $SiO_2$ layer was utilized to apply the $V_G$. All measurements were performed inside a nitrogen ($N_2$)-purged glove box to minimize the adsorption of gas molecules. A light (halogen lamp, Fiber Optic Korea Co., Ltd.) source was placed on top of the probe-station to irradiate the PDs at a distance of 10 cm. The photocurrent was recorded in real-time using LABVIEW program (current vs time frame).

## Supporting Information

Supporting Information is available from the Wiley Online Library or from the author.

## *Acknowledgements*

This work was supported by the Basic Science Research Program (NRF-2016R1 A2B4006395) and the Pioneer Research Center Program (NRF-2016 M3 C1 A3908893) of the National Research Foundation of Korea (NRF) funded by the Korean Ministry of Science and ICT. This work was also supported by the "GRI (GIST Research Institute)" Project through a grant provided by GIST in 2019. J.-K. K and T. L. appreciate the support by the National Creative Research Laboratory program (Grant No. 2012026372) through the NRF funded by the Korean Ministry of Science and ICT.

## *Conflict of Interest*

The authors declare no conflict of interest.

**Keywords:** Molybdenum disulfide · Photodetectors · Silicon dioxide nanoribbons (SNRs) · Transition metal dichalcogenides (TMDs) · Two-dimensional (2D) material

[1] K. S. Novoselov, A. K. Geim, S. V. Morozov, D. Jiang, Y. Zhang, S. V. Dubonos, I. V. Grigorieva, A. A. Firsov, *Science* **2004**, *306*, 666.
[2] K. I. Bolotin, K. J. Sikes, Z. Jiang, M. Klima, G. Fudenberg, J. Hone, P. Kim, H. L. Stormer, *Solid State Commun.* **2008**, *146*, 351.
[3] M. E. Pumarol, M. C. Rosamond, P. Tovee, M. C. Petty, D. A. Zeze, V. Falko, O. V. Kolosov, *Nano Lett.* **2012**, *12*, 2906.
[4] C. Lee, X. Wei, J. W. Kysar, J. Hone, *Science* **2008**, *321*, 385.
[5] S. H. Chae, Y. H. Lee, *Nano Convergence* **2014**, *1*, 15.
[6] G. Pirruccio, L. Martin Moreno, G. Lozano, J. Gomez Rivas, *ACS Nano* **2013**, *7*, 4810.
[7] H. S. Lee, S. W. Min, Y. G. Chang, M. K. Park, T. Nam, H. Kim, J. H. Kim, S. Ryu, S. Im, *Nano Lett.* **2012**, *12*, 3695.
[8] S. Han, R. Bhatia, S. Kim, *Nano Convergence* **2015**, *2*, 17.
[9] J. Brivio, D. T. L. Alexander, A. Kis, *Nano Lett.* **2011**, *11*, 5148.
[10] Q. Tu, I. Spanopoulose, P. Yasaei, C. C. Stoumpos, M. G. Kanatzidis, G. S. Shekhawat, V. P. Dravid, *ACS Nano* **2018**, *12*, 10347.
[11] J. K. Ellis, M. J. Lucero, G. E. Scuseria, *Appl. Phys. Lett.* **2011**, *99*, 261908.
[12] F. H. L. Koppens, T. Mueller, P. Avouris, A. C. Ferrari, M. S. Vitiello, M. Polini, *Nat. Nanotechnol.* **2014**, *9*, 780.
[13] B. Wang, C. Muratore, A. Voevodin, M. A. Haque, *Nano Convergence* **2014**, *1*, 22.
[14] A. Pospischil, T. Mueller, *Appl. Sci. Res.* **2016**, *6*, 78.
[15] Z. Y. Yin, H. Li, H. Li, L. Jiang, Y. M. Shi, Y. H. Sun, G. Lu, Q. Zhang, X. D. Chen, H. Zhang, *ACS Nano* **2012**, *6*, 74.
[16] O. Lopez-Sanchez, D. Lembke, M. Kayci, A. Radenovic, A. Kis, *Nat. Nanotechnol.* **2013**, *8*, 497.
[17] W. Yang, J. Chen, Y. Zhang, Y. Zhang, J. He, X. Fang, *Adv. Funct. Mater.* **2019**, *29*, 1808182.
[18] O. Lopez-Sanchez, E. Alarcon Llado, V. Koman, A. F. I. Morral, A. Radenovic, A. Kis, *ACS Nano* **2014**, *8*, 3042.
[19] L. Z. Hao, Y. J. Liu, W. Gao, Z. D. Han, Q. Z. Xue, H. Z. Zeng, Z. P. Wu, J. Zhu, W. L. Zhang, *J. Appl. Phys.* **2015**, *117*, 114502.
[20] M. L. Tsai, S. H. Su, J. K. Chang, D. S. Tsai, C. H. Chen, C. I. Wu, L. J. Li, L. J. Chen, J. H. He, *ACS Nano* **2014**, *8*, 8317.
[21] A. Pospischil, M. M. Furchi, T. Mueller, *Nat. Nanotechnol.* **2014**, *9*, 257.
[22] H. N. Wang, C. J. Zhang, W. M. Chan, S. Tiwari, F. Rana, *Nat. Commun.* **2015**, *6*, 8831.
[23] B. W. H. Baugher, H. O. H. Churchill, Y. F. Yang, P. Jarillo-Herrero, *Nat. Nanotechnol.* **2014**, *9*, 262.
[24] J. S. Ross, P. Klement, A. M. Jones, N. J. Ghimire, J. Q. Yan, D. G. Mandrus, T. Taniguchi, K. Watanabe, K. Kitamura, W. Yao, D. H. Cobden, X. D. Xu, *Nat. Nanotechnol.* **2014**, *9*, 268.
[25] Y. D. Zhao, K. Xu, F. Pan, C. J. Zhou, F. C. Zhou, Y. Chai, *Adv. Funct. Mater.* **2017**, *27*, 1603484.
[26] Y. Jung, J. Shen, J. Cha, *Nano Convergence* **2014**, *1*, 18.
[27] N. Lim, T. J. Yoo, J. T. Kim, Y. Pak, Y. Kumaresan, H. Kim, W. Kim, B. H. Lee, G. Y. Jung, *RSC Adv.* **2018**, *8*, 9031.
[28] F. Bonaccorso, A. Lombardo, T. Hasan, Z. P. Sun, L. Colombo, A. C. Ferrari, *Mater. Today* **2012**, *15*, 564.
[29] H. Li, Q. Zhang, C. C. R. Yap, B. K. Tay, T. H. T. Edwin, A. Olivier, D. Baillargeat, *Adv. Funct. Mater.* **2012**, *22*, 1385.
[30] K. Dolui, I. Rungger, S. Sanvito, *Phys. Rev. B* **2013**, *87*, 165402.
[31] Y. Kumaresan, Y. Pak, N. Lim, Y. Kim, M. J. Park, S. M. Yoon, H. M. Youn, H. Lee, B. H. Lee, G. Y. Jung, *Sci. Rep.* **2016**, *6*, 37764.
[32] R. Chen, S. Pang, H. An, J. Zhu, S. Ye, Y. Gao, F. Fan, C. Li, *Nat. Energy* **2018**, *3*, 655.
[33] Z. Zhang, Y. Ning, X. Fang, *J. Mater. Chem. C* **2019**, *7*, 223.
[34] Y. Ning, Z. Zhang, F. Teng, X. Fang, *Small* **2018**, *14*, 1703754.
[35] W. Yang, K. Hu, F. Teng, J. Weng, Y. Zhang, X. Fang, *Nano Lett.* **2018**, *18*, 4697.
[36] Y. Zhang, W. Xu, X. Xu, J. Cai, W. Yang, X. Fang, *J. Phys. Chem. Lett.* **2019**, *10*, 836.
[37] M. Yang, T. Y. Kim, T. Lee, S. Hong, *Sci. Rep.* **2018**, *8*, 15822.
[38] D. Kufer, G. Konstantatos, *Nano Lett.* **2015**, *15*, 7307.
[39] W. Kim, A. Javey, O. Vermesh, O. Wang, Y. M. Li, H. J. Dai, *Nano Lett.* **2003**, *3*, 193.

[40] Y. Pak, W. Park, S. Mitra, A. A. S. Devi, K. Loganathan, Y. Kumaresan, Y. Kim, B. Cho, G. Y. Jung, M. M. Hussain, I. S. Roqan, *Small* **2018**, *14*, 1703176.
[41] K. S. Kim, Y. Zhao, H. Jang, S. Y. Lee, J. M. Kim, K. S. Kim, J. H. Ahn, P. Kim, J. Y. Choi, B. H. Hong, *Nature* **2009**, *457*, 706.
[42] J. Xia, X. Huang, L. Z. Liu, M. Wang, L. Wang, B. Huang, D. D. Zhu, J. J. Li, C. Z. Gu, X. M. Meng, *Nanoscale* **2014**, *6*, 8949.
[43] W. J. Zhang, J. K. Huang, C. H. Chen, Y. H. Chang, Y. J. Cheng, L. J. Li, *Adv. Mater.* **2013**, *25*, 3456.
[44] F. Ghasemi, S. Mohajerzadeh, *ACS Appl. Mater. Interfaces* **2016**, *8*, 31179.

Manuscript received: July 5, 2019
Revised manuscript received: August 12, 2019
Accepted manuscript online: August 13, 2019
Version of record online: September 11, 2019